nanomaterials

MDPI

Article

Enhanced Thermoelectric Performance of n-Type Bi_2Se_3 Nanosheets through Sn Doping

Mengyao Li [1], Yu Zhang [1], Ting Zhang [2], Yong Zuo [1,3], Ke Xiao [1], Jordi Arbiol [2,4], Jordi Llorca [5], Yu Liu [6,*] and Andreu Cabot [1,4,*]

1 Catalonia Energy Research Institute—IREC, Sant Adrià de Besòs, 08930 Barcelona, Spain; limengyaorz@gmail.com (M.L.); tingchan99@gmail.com (Y.Z.); yongzuo16@gmail.com (Y.Z.); elvis.xiaoke@gmail.com (K.X.)
2 Catalan Institute of Nanoscience and Nanotechnology (ICN2), CSIC and BIST, Campus UAB, Bellaterra, 08193 Barcelona, Spain; ting.zhang@icn2.cat (T.Z.); arbiol@icrea.cat (J.A.)
3 Istituto Italiano di Tecnologia, Via Morego 30, 16163 Genova, Italy
4 ICREA, Pg. Lluis Companys 23, 08010 Barcelona, Spain
5 Institute of Energy Technologies, Department of Chemical Engineering and Barcelona Research Center in Multiscale Science and Engineering, Universitat Politècnica de Catalunya, EEBE, 08019 Barcelona, Spain; jordi.llorca@upc.edu
6 Institute of Science and Technology Austria (IST Austria), Am Campus 1, 3400 Klosterneuburg, Austria
* Correspondence: yu.liu@ist.ac.at (Y.L.); acabot@irec.cat (A.C.)

Abstract: The cost-effective conversion of low-grade heat into electricity using thermoelectric devices requires developing alternative materials and material processing technologies able to reduce the currently high device manufacturing costs. In this direction, thermoelectric materials that do not rely on rare or toxic elements such as tellurium or lead need to be produced using high-throughput technologies not involving high temperatures and long processes. Bi_2Se_3 is an obvious possible Te-free alternative to Bi_2Te_3 for ambient temperature thermoelectric applications, but its performance is still low for practical applications, and additional efforts toward finding proper dopants are required. Here, we report a scalable method to produce Bi_2Se_3 nanosheets at low synthesis temperatures. We studied the influence of different dopants on the thermoelectric properties of this material. Among the elements tested, we demonstrated that Sn doping resulted in the best performance. Sn incorporation resulted in a significant improvement to the Bi_2Se_3 Seebeck coefficient and a reduction in the thermal conductivity in the direction of the hot-press axis, resulting in an overall 60% improvement in the thermoelectric figure of merit of Bi_2Se_3.

Keywords: thermoelectric; Bi_2Se_3; Sn doping

Citation: Li, M.; Zhang, Y.; Zhang, T.; Zuo, Y.; Xiao, K.; Arbiol, J.; Llorca, J.; Liu, Y.; Cabot, A. Enhanced Thermoelectric Performance of n-Type Bi_2Se_3 Nanosheets through Sn Doping. *Nanomaterials* **2021**, *11*, 1827. https://doi.org/10.3390/nano11071827

Academic Editor: Jiye (James) Fang

Received: 22 June 2021
Accepted: 12 July 2021
Published: 14 July 2021

1. Introduction

Thermoelectric (TE) devices that directly and reversibly convert heat into electricity find unlimited applications [1–6], but their real implementation is hampered by their low cost-effectiveness. The efficiency of energy conversion of a TE device is in part determined by the transport properties of the TE material: Seebeck coefficient S, electrical conductivity σ, and thermal conductivity κ. These material properties are generally grouped into a dimensionless figure of merit, $ZT = S^2\sigma T/\kappa$, where T is the absolute temperature. Efficient TE materials are characterized by high power factors, $S^2\sigma$, and low thermal conductivities, κ. However, the strong correlation between these parameters makes the optimization of the material performance extremely difficult. Several strategies have been developed to maximize ZT, including engineering the electronic band structure of the TE material through doping [7], the use of energy filtering interphases [8], and the reduction in lattice thermal conductivity through the introduction of abundant grain boundaries [9].

Commercial devices use large amounts of highly crystalline Bi_2Te_3-based alloys as the active TE material, which accounts for a significant part of the total cost of the device. To

reduce the device cost, it is critical to develop low-cost materials not relying on scarce Te and low-cost processing strategies not based on high-temperature crystallization from high purity melts. Bi_2Se_3 presents the same structure and similar properties as Bi_2Te_3, and, thus, it is an obvious possible Te-free alternative to Bi_2Te_3. Numerous attempts to improve the *TE* figure of merit of this material have been reported, but with moderate success [10–18].

To maximize the TE performance of a material, one first critical point is to optimize its charge carrier concentration. Three main strategies can be used in this direction: tuning of the material stoichiometry, the introduction of atomic impurities, and/or the introduction of secondary phases able to inject the proper charge carriers to the host material [19–28]. Besides optimizing the charge carrier concentration, it is fundamental to minimize the thermal conductivity using multiscale phonon scattering centers. In this direction, the introduction of atomic impurities and abundant grain boundaries are highly effective. Besides, energy barriers at grain boundaries can also introduce energy- and charge sign-dependent charge carrier scattering, which could result in significant improvements to the Seebeck coefficient [29].

Here, we present a low temperature and high yield, solution-based strategy to prepare Bi_2Se_3 nanomaterials doped with different elements. The influence of different dopants on the TE properties of the material was tested. From the results obtained, we demonstrated Sn to have the highest potential to yield Bi_2Se_3-based materials with improved performance. Thus, we further analyzed the location and chemical state of this element within Bi_2Se_3 and its effect on the material transport properties.

2. Materials and Methods

2.1. Chemicals and Solvents

Polyvinylpyrrolidone (PVP, $(C_6H_9NO)_n$, AMW ~55,000), indium(III) acetate ($InC_6H_9O_6$, 99.99%), and bismuth(III) nitrate pentahydrate ($Bi(NO_3)_3{\cdot}5H_2O$, ≥99.99%) were purchased from Sigma-Aldrich. Sodium selenite (Na_2SeO_3, ≥98%), copper (II) nitrate trihydrate ($Cu(NO_3)_2{\cdot}3H_2O$, 99%), silver nitrate ($AgNO_3$, ≥99.9%), ethylene glycol (EG, $HOCH_2CH_2OH$, 99%), lead (II) acetate trihydrate ($PbC_4H_6O_4{\cdot}3H_2O$), tin(II) chloride anhydrous ($SnCl_2$, 98%), and potassium hydroxide (KOH, ≥98%) were acquired from Fisher. Analytical grade ethanol and acetone were obtained from various sources.

2.2. Synthesis of Bi_2Se_3

Bi_2Se_3 particles were produced following the approach developed by Liu et al., with slight modifications [1]. Bi_2Se_3 (5 mmol), $Bi(NO_3)_3{\cdot}5H_2O$ (10 mmol, 4.851 g), Na_2SeO_3 (15 mmol, 2.594 g), KOH (50 mmol, 2.806 g), and PVP (0.5 g) were first dissolved in a three-neck flask containing EG (200 mL) under an Ar atmosphere at an ambient temperature for 0.5 h. The solution was then heated to 180 °C and kept at this temperature for 3 h. Immediately after the reaction was completed, the solution was allowed to cool naturally to room temperature by removing the heating mantle. The solution was divided into several centrifuge tubes and acetone was added to collect the solid product by centrifugation. In the next step, ethanol was introduced to re-disperse the particles, and acetone was added to precipitate them again. This step was repeated twice. Next, purified Bi_2Se_3 particles were dried under a vacuum overnight at room temperature and kept in the glovebox for posterior use. Around 3 g of particles were obtained per batch.

2.3. Synthesis of $Bi_{2-x}M_xSe_3$

The procedure used to produce $Bi_{2-x}M_xSe_3$ was the same used to produce Bi_2Se_3, but the proper amount of bismuth nitrate was replaced with the corresponding metal precursor, as listed in the chemical section above.

2.4. Nanomaterial Consolidation

Dried Bi_2Se_3 particles were first annealed for 1 h at 350 °C under an Ar flow in a tubular furnace. Then, the annealed material was introduced into a graphite die and

consolidated into cylinders (Ø 10 mm × 10 mm) at 480 °C and 50 MPa of pressure for 4 min with a custom-made hot press. The relative densities of the compacted pellets were measured by Archimedes' method. To measure transport properties in the two relevant directions, cylindrical pellets were cut into ca. 8 × 6 × 1 mm rectangular bars along the pressure axis, and 1 mm thick disks along the perpendicular to the pressure axis.

2.5. Structural and Chemical Characterization

The field emission scanning electron microscope (SEM) was used to determine the nanoparticle morphology on an Auriga Zeiss. An Oxford energy dispersive X-ray spectrometer (EDX) was used to measure the material composition at 20.0 kV. X-ray diffraction (XRD) was performed on a Bruker AXS D8 Advance diffractometer. The crystal structure of the samples was analyzed under the 200 keV Tecnai F20 field emission microscope equipped with a Gatan quantum image filter. X-ray photoelectron spectroscopy (XPS) was performed on a Specs system with the material inside the chamber at a pressure below 10^{-7} Pa. Data processing was carried out using the CasaXPS program.

2.6. Performance Characterization of Bulk Nanomaterial

Seebeck coefficients and resistivities were measured by the static direct current method and by the standard four-probe method, respectively, in an LSR-3 Linseis system under helium. All samples were tested for at least three heating and cooling cycles. Considering the system accuracy and measurement accuracy, the measurement error of the conductivity and Seebeck coefficient was estimated to be about 4%. Thermal diffusivity (λ), constant pressure heat capacity (C_p), and density of the material (ρ) were used to obtain the thermal conductivities (κ_{total}), where $\kappa_{total} = \lambda C_p \rho$. The thermal diffusivities of the samples were measured by a Xenon Flash Apparatus XFA600, which has an estimated error of ca. 5%. We used a constant as the heat capacity (C_p), which was estimated from empirical formulas by the Dulong–Petit limit (3R law). Under a magnetic field of 0.6 T, the Hall charge carrier concentrations and mobilities at room temperature were measured by the Van der Pauw method. The figures in this article do not have error bars in order to avoid cluttering the plots.

3. Results and Discussion

Following the above synthesis method, Bi_2Se_3 nanosheets grouped into flower-like particles were produced, as shown by the SEM micrographs (Figure 1a,b). Bi_2Se_3 shows a screw dislocation growth mechanism (Figure 1c). This layer-by-layer growth mechanism is usually due to the low supersaturation in the synthesis conditions, which inhibits dendritic growth. Axial screw dislocation is the self-sustaining spiral growth of nanosheets around the axis [15,23].

The XRD analysis showed that the crystal structure of the obtained nanosheets matched the rhombohedral Bi_2Se_3 phase (Figure 1d, JCPDS No. 00-033-0214). Figure 1e shows the layered rhombohedral crystal structure of Bi_2Se_3, which consists of five covalently bonded atomic planes of Se-Bi-Se-Bi-Se. Quintuple layers are weakly bonded by van der Waals. The HRTEM characterization showed that the material has good crystallinity and has a crystal phase consistent with the Bi_2Se_3 rhombohedral phase (space group = R3-MH) with a = b = 4.1340 Å and c = 28.6300 Å (Figure 1f,g).

Nanosheets were annealed at 350 °C, and the annealed powder was hot-pressed into cylindrical pellets with a diameter of 10 mm and a height of 10 mm in a glovebox filled with argon. Samples were hot-pressed for four minutes at 480 °C and 50 MPa, and then naturally cooled to an ambient temperature. The relative density of the cylinders produced by this process was about 93% of the theoretical value. From the consolidated cylinder, a rectangular bar of 8 × 6 × 1 mm was cut longitudinally, and a 1 mm thick pellet was cut transversely (Figure 2). These samples were used to measure the TE properties of materials parallel to the pressure axis (//) and perpendicular to the pressure axis (⊥).

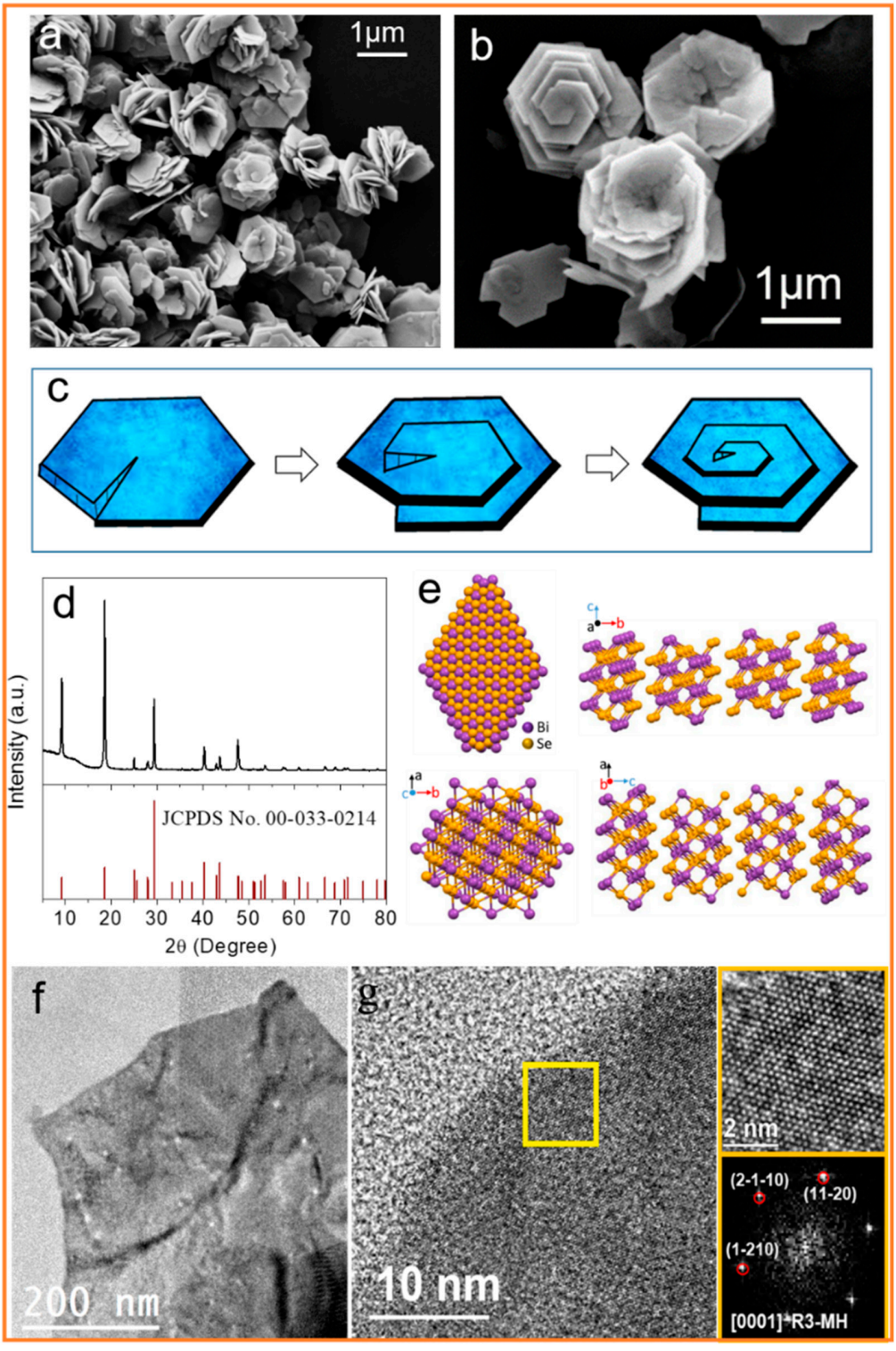

Figure 1. (**a**,**b**) SEM micrographs of the Bi_2Se_3 particles. (**c**) Scheme of the screw dislocation growth mechanism. (**d**) The XRD pattern of the Bi_2Se_3 particles. (**e**) The layered rhombohedral crystal structure of Bi_2Se_3. (**f**) A low-resolution TEM image. (**g**) An HRTEM micrograph of the Bi_2Se_3 particles and its corresponding power spectrum. From the crystallographic domain, the Bi_2Se_3 lattice fringe distances were measured to be 0.205 nm, 0.205 nm, and 0.204 nm, at 60.96° and 120.86°, respectively, which could be illuminated as the rhombohedral Bi_2Se_3 phase, visualized along the [0001] zone axis.

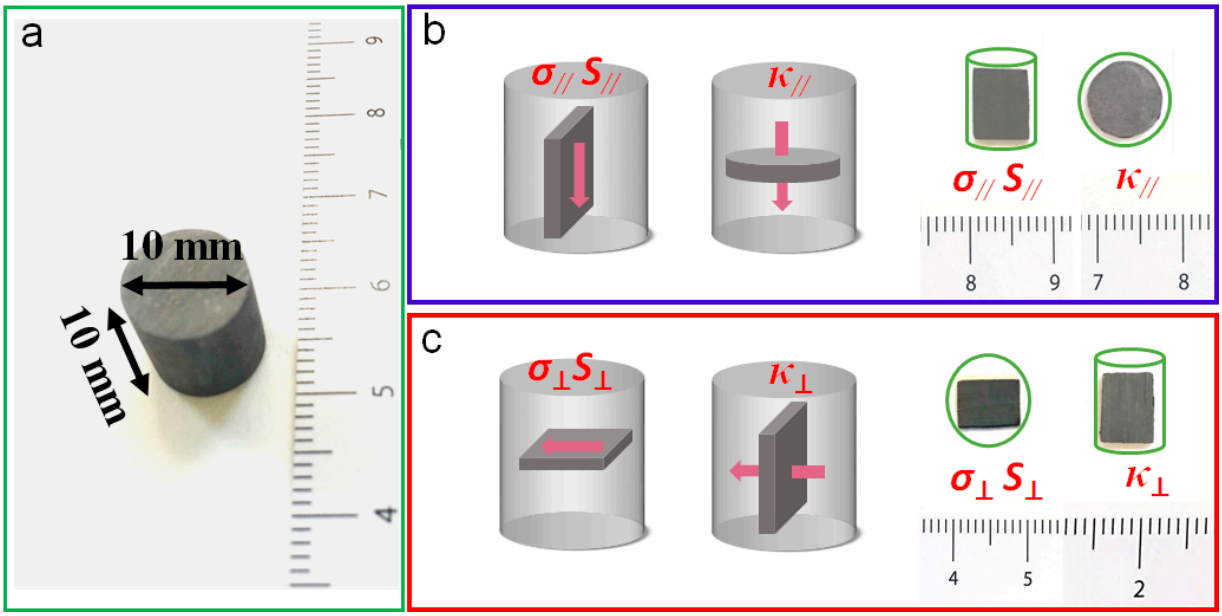

Figure 2. (**a**) Photograph of the consolidated Bi_2Se_3 cylinder. (**b**,**c**) Scheme and images of the samples used to measure the material transport properties in the directions parallel (**b**) and vertical (**c**) to the pressure axis.

Figure 3 displays the electrical conductivity (σ), Seebeck coefficient (S), and power factor ($PF = S^2\sigma$) of the $Bi_{2-x}M_xSe_3$ (M = Sn, Cu, Ag, Pb, In) pellets perpendicular to the press direction. The electrical conductivity of the undoped material decreased with temperature, which pointed to a degenerated semiconductor behavior. Compared to the undoped material, the electrical conductivity of all the doped samples was slightly lower, except for the Ag-doped samples. On the other hand, the samples doped with Sn and to a minor extent, Pb displayed an increase in the absolute value of the Seebeck coefficient. Overall, the highest power factors were obtained with the Sn doping. Thus, we decided to further study the effect of this element.

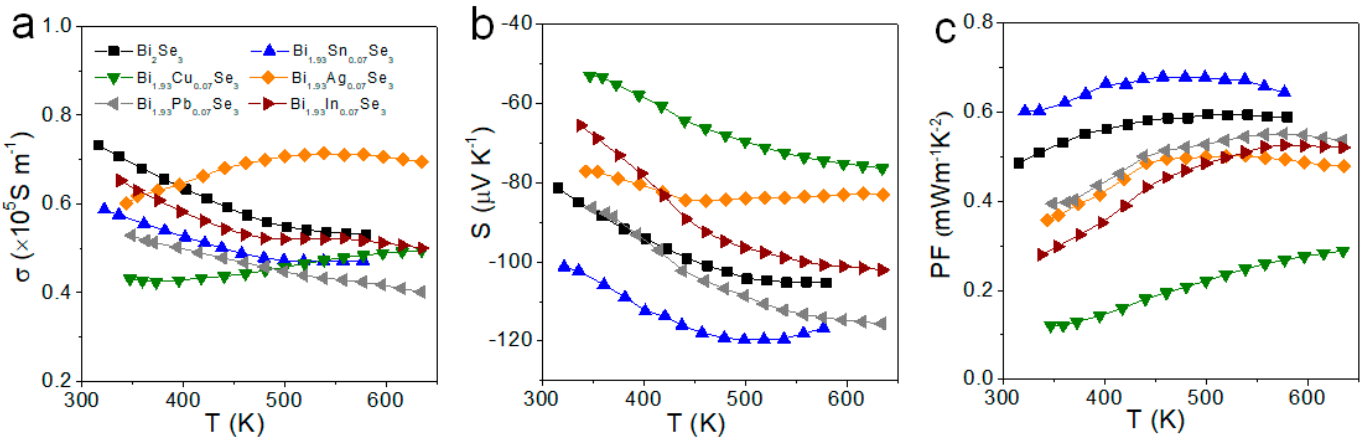

Figure 3. TE properties of $Bi_{2-x}M_xSe_3$ (M = Sn, Cu, Ag, Pb, In) samples measured perpendicular to the press direction: (**a**) electrical conductivity, σ; (**b**) Seebeck coefficient, S; (**c**) power factor, PF.

Figure 4 displays the electrical conductivity, Seebeck coefficient, and power factor of $Bi_{2-x}Sn_xSe_3$ materials containing different amounts of Sn. We observed that the electrical conductivity decreased and the absolute value of the Seebeck coefficient increased with the amount of Sn up to a certain Sn concentration. The highest power factors were finally obtained for $Bi_{1.93}Sn_{0.07}Se_3$. The decrease in the electrical conductivity and increase in

the absolute value of the Seebeck coefficient denoted a reduction in the charge carrier concentration, which points to the presence of Sn^{2+} ions instead of Sn^{4+} at Bi^{3+} sites.

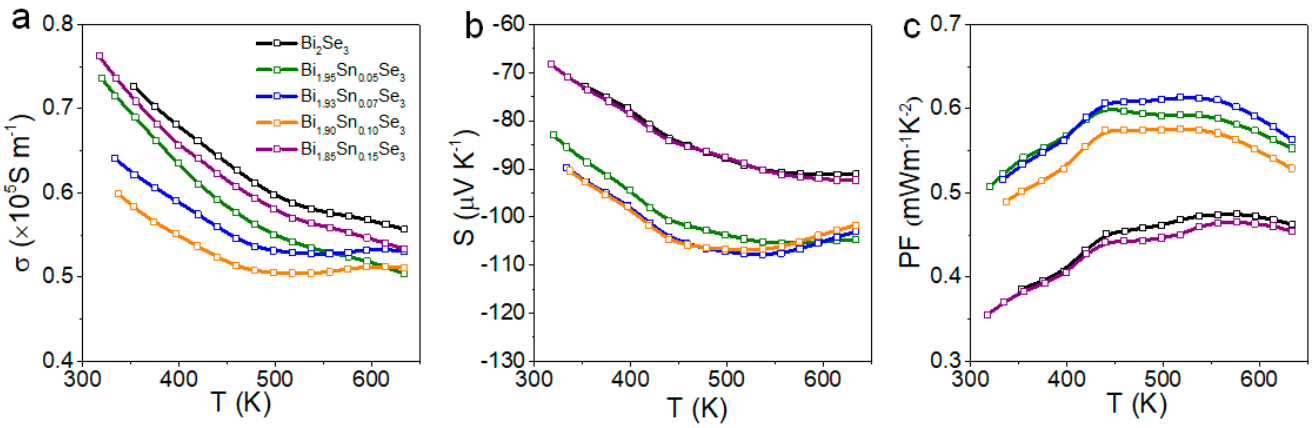

Figure 4. Thermoelectric properties of $Bi_{2-x}Sn_xSe_3$ perpendicular to the press direction: (**a**) electrical conductivity, σ; (**b**) Seebeck coefficient, S; (**c**) power factor, PF.

Figure 5 shows representative SEM micrographs of the $Bi_{1.93}Sn_{0.07}Se_3$ particles, which had similar sizes but did not display the flower-like morphology observed from Bi_2Se_3. As shown in Figure 6, the XRD characterization confirmed that the $Bi_{1.93}Sn_{0.07}Se_3$ particles maintained their rhombohedral structure. With the introduction of Sn, the XRD peaks shifted to lower 2θ angles, suggesting the incorporation of Sn within the Bi_2Se_3 lattice [5].

The HRTEM characterization confirmed the rhombohedral phase of the $Bi_{1.93}Sn_{0.07}Se_3$ particles (Figure 7a). EELS chemical composition maps obtained from the red squared region in the HAADF STEM micrograph shown in Figure 7b displayed a homogeneous distribution of Sn, Bi and Se within the $Bi_{1.93}Sn_{0.07}Se_3$ nanosheet.

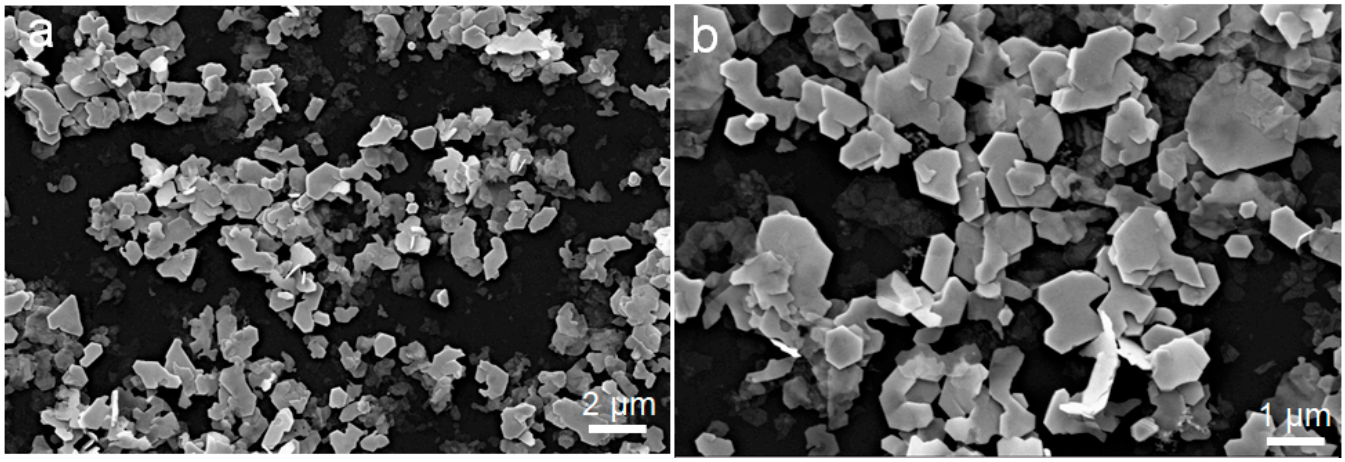

Figure 5. SEM micrographs of $Bi_{1.93}Sn_{0.07}Se_3$ nanosheets with different magnifications; (**a**) magnification 5.00 K ×, (**b**) magnification 10.00 K ×.

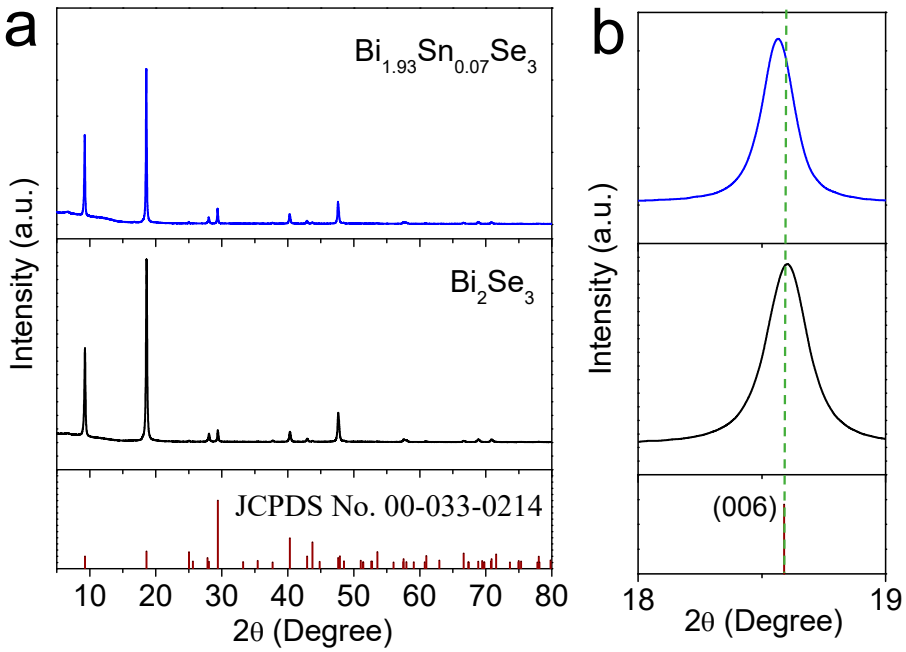

Figure 6. (**a**) XRD patterns of Bi_2Se_3 and $Bi_{1.93}Sn_{0.07}Se_3$; (**b**) expansion diagram of the area corresponding to the diffraction peak of Bi_2Se_3 (006).

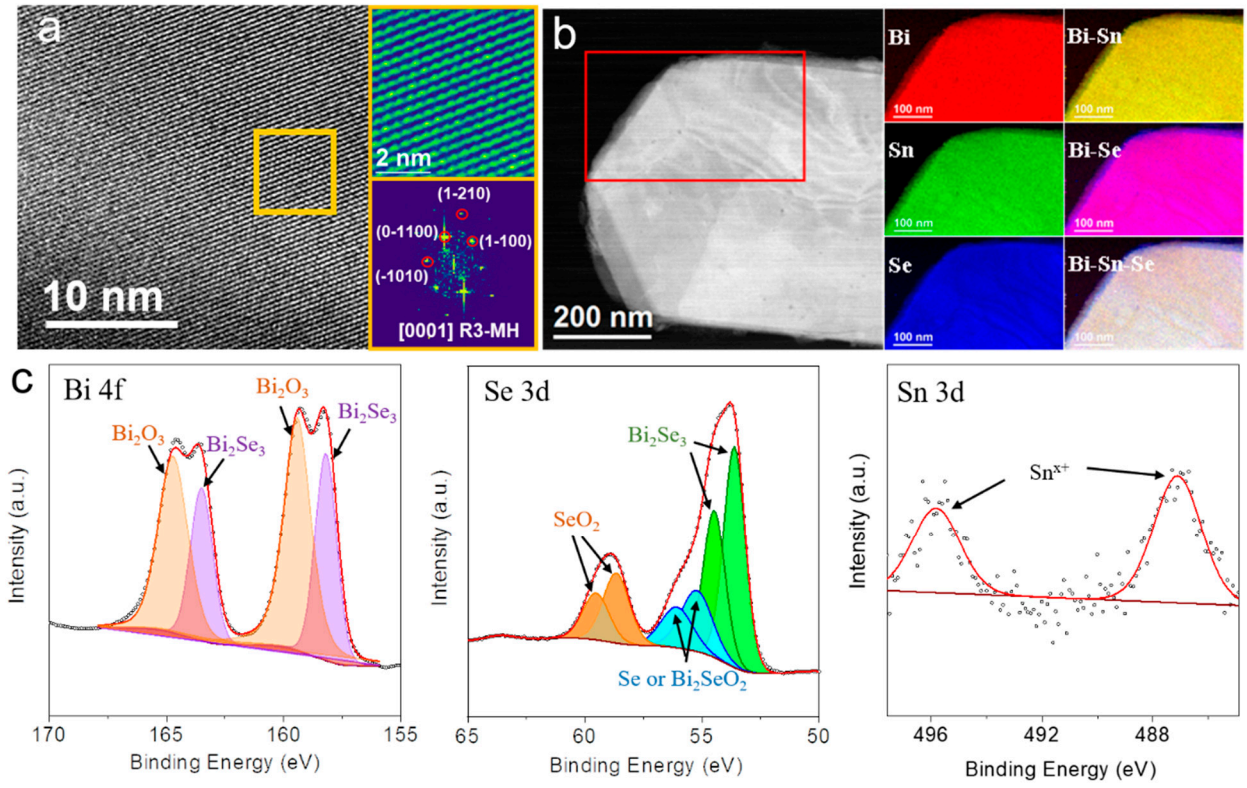

Figure 7. (**a**) An HRTEM micrograph of a $Bi_{1.93}Sn_{0.07}Se_3$ nanosheet, detailed information of the orange squared area and its corresponding power spectrum. Bi_2Se_3 lattice fringe distances were measured to be 0.370 nm, 0.349 nm, 0.202 nm, and 0.351 nm, at 62.89°, 92.61° and 122.99°, respectively, which could be illuminated as the rhombohedral Bi_2Se_3 phase, along its [0001] zone axis. (**b**) EELS chemical composition maps obtained from the red squared area of the STEM micrograph. Individual Bi $N_{2,3}$-edges at 679 eV (red), Sn $M_{4,5}$-edges at 485 eV (green), Se $M_{2,3}$-edges at 162 eV (blue) and composites of Bi-Sn, Bi-Se as well as Bi-Sn-Se. (**c**) Bi 4f, Se 3d and Sn 3d high-resolution XPS spectra obtained from $Bi_{1.93}Sn_{0.07}Se_3$ nanosheets.

Bi 4f, Se 3d and Sn 3d high-resolution XPS spectra of $Bi_{1.93}Sn_{0.07}Se_3$ particles are displayed in Figure 7c. The high-resolution Bi 4f spectrum was fitted with two doublets, associated with Bi^{3+} within a Bi_2Se_3 chemical environment (Bi $4f_{7/2}$ at 158.2 eV) and Bi within a more electronegative environment, as it could be Bi_2O_3 or Bi_2SeO_2 (Bi $4f_{7/2}$ at 159.4 eV) [30]. This oxidation of the particles surface is related to their transport and handling in the air [4]. The high-resolution Se 3d XPS spectrum was fitted with three doublets, corresponding to Se within the Bi_2Se_3 (Se $3d_{5/2}$ at 53.6 eV), selenium in an elemental or Bi_2SeO_2 environment (Se $3d_{5/2}$ at 55.2 eV), probably arising from the partial oxidation of the material surface, and Se in a SeO_2 chemical environment (Se $3d_{5/2}$ at 58.6 eV) [30,31]. Finally, the high-resolution Sn 3d XPS spectrum was difficult to fit owing to the small amount of this element, but the broadness of the peaks pointed to the presence of at least two Sn chemical states that should be tentatively assigned to Sn^{x+} within a SnSe and an oxidized environment [31]. According to the electrical properties measured at the introduction of Sn, we tentatively assigned the Sn^{x+} component within SnSe to Sn^{2+}.

Top-view and cross-section SEM micrographs of Bi_2Se_3 and $Bi_{1.93}Sn_{0.07}Se_3$ (Figure 8) showed the final pellets presenting a laminar microstructure with an evident preferential orientation of the material layers. Bi_2Se_3 displayed larger and thinner layers than $Bi_{1.93}Sn_{0.07}Se_3$. When comparing the XRD patterns of the sample held in two normal directions, parallel and perpendicular to the pressure axis (Figure 8e,f), we observed that the relative XRD peak intensity clearly differed. This result confirmed the preferential crystallographic orientation of the hot-pressed materials, with the [001] crystallographic direction oriented parallel to the pressure axis.

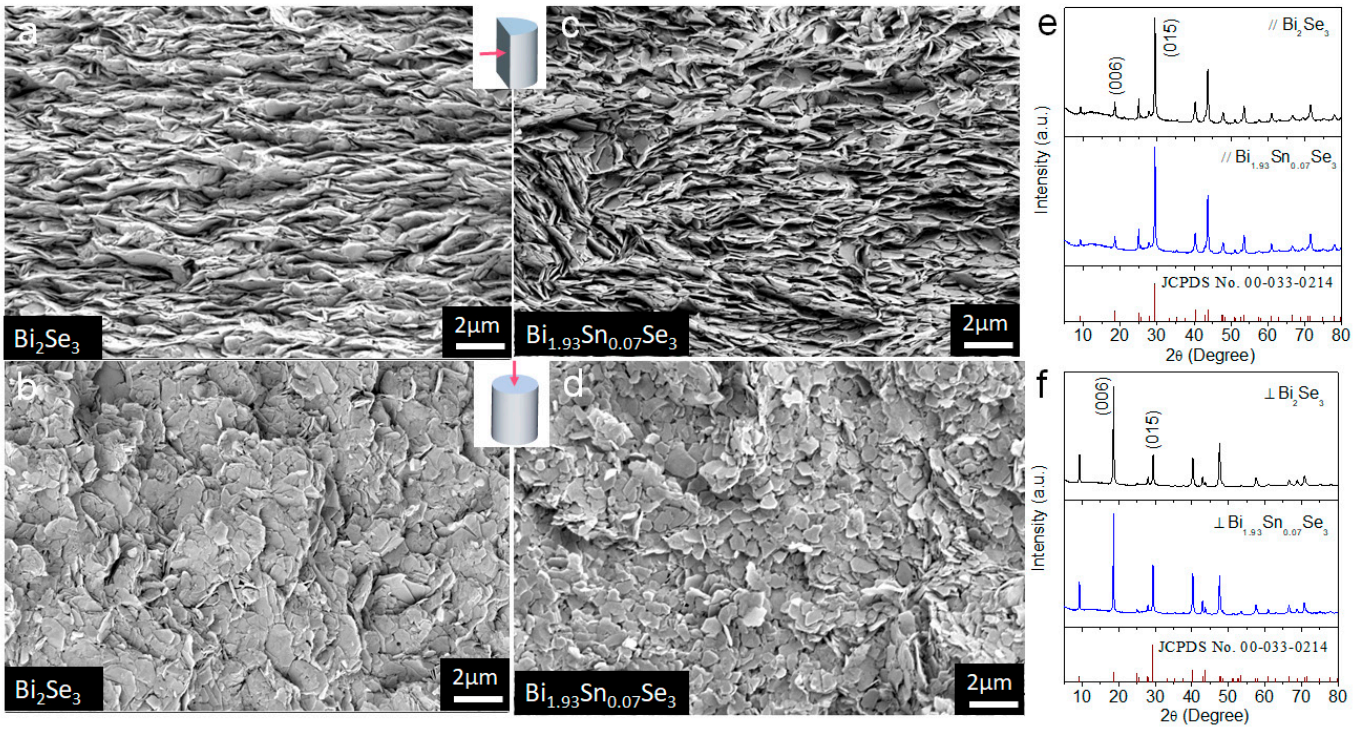

Figure 8. (**a**,**b**) Cross-section and top-view SEM micrograph of Bi_2Se_3. (**c**,**d**) Cross-section and top-view SEM micrograph of $Bi_{1.93}Sn_{0.07}Se_3$. (**e**,**f**) XRD patterns of Bi_2Se_3 and $Bi_{1.93}Sn_{0.07}Se_3$ measured in two perpendicular directions, along (//) and perpendicular (⊥) to the pressure axis.

Figure 9 displays the TE properties of Bi_2Se_3 and $Bi_{1.93}Sn_{0.07}Se_3$ measured in the two directions. We observed $\sigma_{\perp} > \sigma_{//}$, as expected from the higher charge carrier mobilities in the *ab* crystal plane compared with the *c* direction, and the extended size of the crystal domains in the direction normal to the pressure direction within the layered pellets. On

the other hand, similar Seebeck coefficients were obtained in both directions, pointing out that this parameter has little relationship with grain boundary scattering in this material.

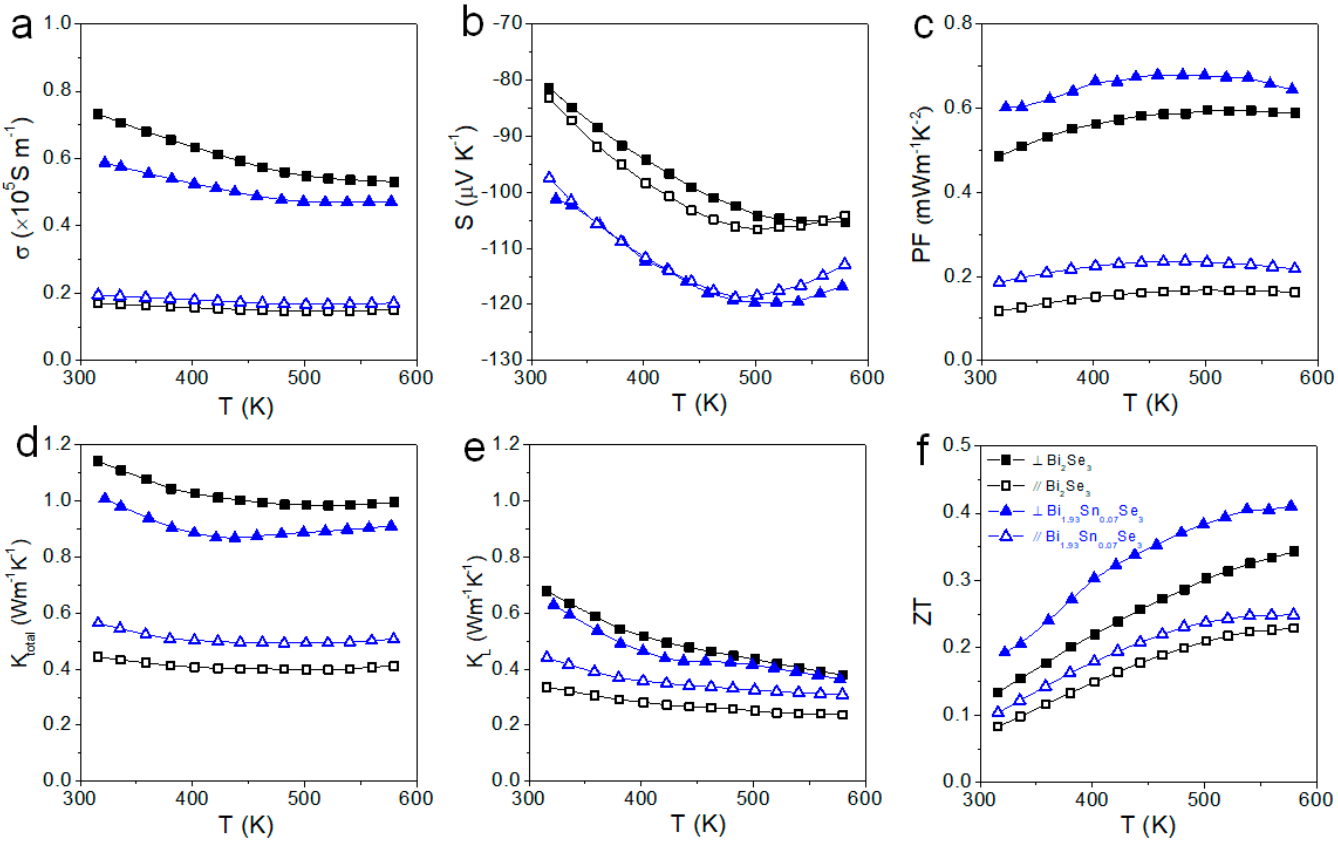

Figure 9. TE properties of Bi_2Se_3 and $Bi_{1.93}Sn_{0.07}Se_3$ parallel (//) and vertical (⊥) to the pressure axis: (**a**) electrical conductivity, σ; (**b**) Seebeck coefficient, S; (**c**) power factor, PF; (**d**) total thermal conductivity, κ; (**e**) lattice thermal conductivity, κ_L; and (**f**) the TE figure of merit, ZT.

When comparing the TE properties of Bi_2Se_3 and $Bi_{1.93}Sn_{0.07}Se_3$, we observed $\sigma_{\perp}$ to slightly increase and $\sigma_{//}$ to slightly decrease with the introduction of Sn, which could be in part related to the thinner and larger material layers observed within the layered Bi_2Se_3 pellets compared with $Bi_{1.93}Sn_{0.07}Se_3$. On the other hand, with the introduction of Sn, S increased in both directions, which resulted in a higher PF in both directions for the $Bi_{1.93}Sn_{0.07}Se_3$ sample.

Table 1 displays the Hall charge carrier concentration and mobility of Bi_2Se_3 and $Bi_{1.93}Se_{0.07}Se_3$ pellets at room temperature. As expected from the electrical conductivity and Seebeck coefficient measurements, we observed the Sn introduction to result in a decrease in the charge carrier concentration, from $n_H = 1.8 \times 10^{19}$ cm^{-3} for Bi_2Se_3 to $n_H = 1.3 \times 10^{19}$ cm^{-3} for $Bi_{1.93}Se_{0.07}Se_3$. This result is consistent with the presence of Sn^{2+} replacing Bi^{3+} ions, thus trapping a free electron. We believe this optimization of the charge carrier concentration to be at the origin of the higher PF obtained with the introduction of Sn. We further calculated the effective mass of the Bi_2Se_3 and $Bi_{1.93}Sn_{0.07}Se_3$ materials using a single parabolic band (SPB) model. For detailed calculations, the carrier transport property analysis included [32]:

Table 1. Room temperature transport properties and m^* of the Bi_2Se_3 and $Bi_{1.93}Se_{0.07}Se_3$ pellets.

Materials	n_H [10^{19} cm^{-3}]	μ_H [cm^2 V^{-1} S^{-1}]	m^*/m_0
Bi_2Se_3	1.77	178.6	0.27
$Bi_{1.93}Sn_{0.07}Se_3$	1.34	239.3	0.29

The Seebeck coefficient,

$$S(\eta) = \frac{\kappa_B}{e}\left[\frac{(r+5/2)\cdot F_{r+3/2}(\eta)}{(r+3/2)\cdot F_{r+1/2}(\eta)} - \eta\right] \quad (1)$$

The Hall carrier concentration,

$$n_H = \frac{1}{e\cdot R_H} = \frac{(2m^*\cdot\kappa_B T)^{3/2}}{3\pi^2\hbar^3}\cdot\frac{(r+3/2)^2\cdot F^2_{r+1/2}(\eta)}{(2r+3/2)\cdot F_{2r+1/2}(\eta)} \quad (2)$$

The Hall mobility,

$$\mu_H = \left[\frac{e\pi\hbar^4}{\sqrt{2}(\kappa_B T)^{3/2}}\frac{C_l}{E_{def}{}^2(m^*)^{5/2}}\right]\frac{(2r+3/2)\cdot F_{2r+1/2}(\eta)}{(r+3/2)^2\cdot F_{r+1/2}(\eta)} \quad (3)$$

where $F_x(\eta) = \int_0^\infty \frac{\varepsilon^x}{1+e^{(\varepsilon-\eta)}}d\varepsilon$ is the Fermi integral.

In the above equations, S, μ_H, η, κ_B, e, r, R_H, $\hbar$, C_l, E_{def}, and m^* are the Seebeck coefficient, the carrier mobility, the reduced Fermi level, the Boltzmann constant, the electron charge, the carrier scattering factor ($r = -1/2$ for acoustic phonon scattering), the Hall coefficient, the reduced plank constant, the elastic constant for longitudinal vibrations, the deformation potential coefficient, and the density of state effective mass, respectively. Using the experimental S, the reduced Fermi level η can be obtained by Equation (1). Substituting the estimated η and the measured "n_H" and "μ_H" into Equations (2) and (3), the effective mass "m^*" can be calculated. The results show that m^* increased slightly with the Sn doping (Table 1).

Consistent with the layered structure of the pellets and their crystallographic texture, the thermal conductivity of the materials measured in the direction normal to the pressure axis was much higher than in the pressure axis, $\kappa_\perp > \kappa_{//}$. The introduction of Sn resulted in lower $\kappa_\perp$ but higher $\kappa_{//}$ values, which is related to the different microstructure of the layers, with thicker and smaller $Bi_{1.93}Se_{0.07}Se_3$ plates compared to those within the Bi_2Se_3 pellet.

Overall, the $Bi_{1.93}Sn_{0.07}Se_3$ samples measured in the pellet plane displayed the highest PF and ZT values, 0.65 m Wm^{-1} K^{-2} and 0.41, respectively. These values are among the highest published for Bi_2Se_3-based materials, as displayed in Table 2.

Table 2. A comprehensive summary of the thermoelectric performance of the previously reported Bi_2Se_3.

	ZT at Room Temperature				ZT_{max}			
Materials	**σ (10^4S/m)**	**S (μV/K)**	**κ (W/mK)**	**ZT**	**σ (10^4 S/m)**	**S (μV/K)**	**κ (W/mK)**	**ZT**
$K_{2.5}Bi_{8.5}Se_{14}$ [33]	0.4	−100	0.6	0.05	1.8	−160	0.38	1 (873 K)
$Bi_{0.7}Sb_{0.3}Se$ [34]	4.5	−138	0.5	0.45	4.2	−160	0.7	0.8 (425 k)
$Bi_{5.6}Sb_{2.4}Se_7$ [35]					4.8	−168.5	0.73	0.55 (300 K)
Bi_2Se_3 [28]	2	−120	0.5	0.17	1.95	−155	0.4	0.48 (427 K)
Bi_2Se_3 [21]	1.78	−90	0.42	0.1	3	−120.7	0.49	0.35 (400 K)
Bi_2Se_3 $HA_{0.11}DMSO_{0.06}$ [36]	14.8	−80	1.52	0.187				
Bi_2Se_3 [12]	2.5	−60	0.55	0.05	2	−100	0.6	0.18 (480 K)
$Cu_{0.1}Bi_2Se_3$ [37]					1.46	−84	0.32	0.1 (290 K)
Bi_2Se_3 [20]	0.212	−115	0.75	0.011	0.6755	−150	0.83	0.096 (523 K)
This work	**5.87**	**−101**	**1**	**0.195**	**4.72**	**−116**	**0.91**	**0.41** (577 K)

4. Conclusions

We report here a large-scale method to synthesize n-type Bi_2Se_3 nanosheets with different dopants. Samples doped with Sn provided the highest TE performances. The composition was optimized at $Bi_{1.93}Se_{0.07}Se_3$. Upon Sn doping, we observed an increase in the Seebeck coefficient and the power factor compared to pure Bi_2Se_3. As a result, a

power factor up to 0.65 m $Wm^{-1}K^{-2}$ and a ZT of 0.41 were obtained for the $Bi_{1.93}Sn_{0.07}Se_3$ pellet measured in the direction perpendicular to the pressure axis, which represents a 60% increase over pure Bi_2Se_3.

Author Contributions: Conceptualization, M.L.; methodology, M.L. and Y.L.; software, M.L. and Y.Z. (Yong Zuo); formal analysis, M.L., J.A. and J.L.; data curation, T.Z., Y.Z. (Yu Zhang) and K.X.; writing—original draft preparation, M.L.; writing—review and editing, A.C.; supervision, Y.L., A.C. All authors have read and agreed to the published version of the manuscript.

Funding: All sources of funding are acknowledged in the acknowledgements section.

Data Availability Statement: Data are contained within the article.

Acknowledgments: M.L., Y.Z., T.Z. and K.X. thank the China Scholarship Council for their scholarship support. Y.L. acknowledges funding from the European Union's Horizon 2020 research and innovation program under the Marie Sklodowska-Curie grant agreement No. 754411. J.L. thanks the ICREA Academia program and projects MICINN/FEDER RTI2018-093996-B-C31 and G.C. 2017 SGR 128. ICN2 acknowledges funding from the Generalitat de Catalunya 2017 SGR 327 and the Spanish MINECO ENE2017-85087-C3.

Conflicts of Interest: The authors declare no conflict of interest.

References

1. Liu, Y.; Zhang, Y.; Lim, K.H.; Ibáñez, M.; Ortega, S.; Li, M.; David, J.; Martí-Sànchez, S.; Ng, K.M.; Arbiol, J.; et al. High Thermoelectric Performance in Crystallographically Textured n type $Bi_2Te_{3-x}Se_x$ Produced from Asymmetric Colloidal Nanocrystals. *ACS Nano* **2018**, *12*, 7174–7184. [CrossRef]
2. Liu, Y.; Zhang, Y.; Ortega, S.; Ibáñez, M.; Lim, K.H.; Grau-Carbonell, A.; Martí-Sánchez, S.; Ng, K.M.; Arbiol, J.; Kovalenko, M.V.; et al. Crystallographically Textured Nanomaterials Produced from the Liquid Phase Sintering of $Bi_xSb_{2-x}Te_3$ Nanocrystal Building Blocks. *Nano Lett.* **2018**, *18*, 2557–2563. [CrossRef]
3. Zhang, Y.; Liu, Y.; Lim, K.H.; Xing, C.; Li, M.; Zhang, T.; Tang, P.; Arbiol, J.; Llorca, J.; Ng, K.M.; et al. Tin Diselenide Molecular Precursor for Solution-Processable Thermoelectric Materials. *Angew. Chem.* **2018**, *130*, 17309–17314. [CrossRef]
4. Li, M.; Liu, Y.; Zhang, Y.; Han, X.; Zhang, T.; Zuo, Y.; Xie, C.; Xiao, K.; Arbiol, J.; Llorca, J.; et al. Effect of the Annealing Atmosphere on Crystal Phase and Thermoelectric Properties of Copper Sulfide. *ACS Nano* **2021**, *15*, 4967–4978. [CrossRef] [PubMed]
5. Li, M.; Liu, Y.; Zhang, Y.; Zuo, Y.; Li, J.; Lim, K.H.; Cadavid, D.; Ng, K.M.; Cabot, A. Crystallographically textured SnSe nanomaterials produced from the liquid phase sintering of nanocrystals. *Dalt. Trans.* **2019**, *48*, 3641–3647. [CrossRef] [PubMed]
6. Ortega, S.; Ibáñez, M.; Liu, Y.; Zhang, Y.; Kovalenko, M.V.; Cadavid, D.; Cabot, A. Bottom-up engineering of thermoelectric nanomaterials and devices from solution-processed nanoparticle building blocks. *Chem. Soc. Rev.* **2017**, *46*, 3510–3528. [CrossRef] [PubMed]
7. Ibañez, M.; Hasler, R.; Genc, A.; Liu, Y.; Kuster, B.; Schuster, M.; Dobrozhan, O.; Cadavid, D.; Arbiol, J.; Cabot, A.; et al. Ligand-mediated band engineering in bottom-up assembled SnTe nanocomposites for thermoelectric energy conversion. *J. Am. Chem. Soc.* **2019**, *141*, 8025–8029. [CrossRef] [PubMed]
8. Zhang, Y.; Xing, C.; Liu, Y.; Li, M.; Xiao, K.; Guardia, P.; Lee, S.; Han, X.; Ostovari Moghaddam, A.; Josep Roa, J.; et al. Influence of copper telluride nanodomains on the transport properties of n-type bismuth telluride. *Chem. Eng. J.* **2021**, *418*, 129374. [CrossRef]
9. Ibáñez, M.; Genç, A.; Hasler, R.; Liu, Y.; Dobrozhan, O.; Nazarenko, O.; De La Mata, M.; Arbiol, J.; Cabot, A.; Kovalenko, M.V. Tuning transport properties in thermoelectric nanocomposites through inorganic ligands and heterostructured building blocks. *ACS Nano* **2019**, *13*, 6572–6580. [CrossRef]
10. Wang, S.; Sun, Y.; Yang, J.; Duan, B.; Wu, L.; Zhang, W.; Yang, J. High thermoelectric performance in Te-free $(Bi,Sb)_2Se_3$: Via structural transition induced band convergence and chemical bond softening. *Energy Environ. Sci.* **2016**, *9*, 3436–3447. [CrossRef]
11. Min, Y.; Park, G.; Kim, B.; Giri, A.; Zeng, J.; Roh, J.W.; Kim, S.I.; Lee, K.H.; Jeong, U. Synthesis of Multishell Nanoplates by Consecutive Epitaxial Growth of Bi_2Se_3 and Bi_2Te_3 Nanoplates and Enhanced Thermoelectric Properties. *ACS Nano* **2015**, *9*, 6843–6853. [CrossRef]
12. Min, Y.; Roh, J.W.; Yang, H.; Park, M.; Kim, S.I.; Hwang, S.; Lee, S.M.; Lee, K.H.; Jeong, U. Surfactant-free scalable synthesis of Bi_2Te_3 and Bi_2Se_3 nanoflakes and enhanced thermoelectric properties of Their Nanocomposites. *Adv. Mater.* **2013**, *25*, 1425–1429. [CrossRef]
13. Liu, W.; Lukas, K.C.; McEnaney, K.; Lee, S.; Zhang, Q.; Opeil, C.P.; Chen, G.; Ren, Z. Studies on the Bi_2Te_3-Bi_2Se_3-Bi_2S_3 system for mid-temperature thermoelectric energy conversion. *Energy Environ. Sci.* **2013**, *6*, 552–560. [CrossRef]
14. Le, P.H.; Wu, K.H.; Luo, C.W.; Leu, J. Growth and characterization of topological insulator Bi_2Se_3 thin films on $SrTiO_3$ using pulsed laser deposition. *Thin Solid Films* **2013**, *534*, 659–665. [CrossRef]
15. Morin, S.A.; Forticaux, A.; Bierman, M.J.; Jin, S. Screw Dislocation-Driven Growth of 2D Nanoplates. *Nano Lett.* **2011**, *11*, 4449–4455. [CrossRef]

16. Janíček, P.; Drašar, Č.; Beneš, L.; Lošták, P. Thermoelectric properties of Tl-doped Bi_2Se_3 single crystals. *Cryst. Res. Technol.* **2009**, *44*. [CrossRef]
17. Cui, H.; Liu, H.; Li, X.; Wang, J.; Han, F.; Zhang, X.; Boughton, R.I. Synthesis of Bi_2Se_3 thermoelectric nanosheets and nanotubes through hydrothermal co-reduction method. *J. Solid State Chem.* **2004**, *177*, 4001–4006. [CrossRef]
18. Bauer, C.; Veremchuk, I.; Kunze, C.; Benad, A.; Dzhagan, V.M.; Haubold, D.; Pohl, D.; Schierning, G.; Nielsch, K.; Lesnyak, V.; et al. Heterostructured Bismuth Telluride Selenide Nanosheets for Enhanced Thermoelectric Performance. *Small Sci.* **2021**, *1*, 2000021. [CrossRef]
19. Zhang, J.; Peng, Z.; Soni, A.; Zhao, Y.; Xiong, Y.; Peng, B.; Wang, J.; Dresselhaus, M.S.; Xiong, Q. Raman spectroscopy of few-quintuple layer topological insulator Bi_2Se_3 nanoplatelets. *Nano Lett.* **2011**, *11*, 2407–2414. [CrossRef]
20. Kadel, K.; Kumari, L.; Li, W.Z.; Huang, J.Y.; Provencio, P.P. Synthesis and Thermoelectric Properties of Bi_2Se_3 Nanostructures. *Nanoscale Res. Lett.* **2011**, *6*, 1–7. [CrossRef]
21. Sun, Y.; Cheng, H.; Gao, S.; Liu, Q.; Sun, Z.; Xiao, C.; Wu, C.; Wei, S.; Xie, Y. Atomically thick bismuth selenide freestanding single layers achieving enhanced thermoelectric energy harvesting. *J. Am. Chem. Soc.* **2012**, *134*, 20294–20297. [CrossRef]
22. Pei, Y.; Wang, H.; Snyder, G.J. Band engineering of thermoelectric materials. *Adv. Mater.* **2012**, *24*, 6125–6135. [CrossRef]
23. Zhuang, A.; Li, J.J.; Wang, Y.C.; Wen, X.; Lin, Y.; Xiang, B.; Wang, X.; Zeng, J. Screw-dislocation-driven bidirectional spiral growth of Bi_2Se_3 nanoplates. *Angew. Chem.* **2014**, *53*, 6425–6429. [CrossRef] [PubMed]
24. Kim, S.J.; We, J.H.; Cho, B.J. A wearable thermoelectric generator fabricated on a glass fabric. *Energy Environ. Sci.* **2014**, *7*, 1959–1965. [CrossRef]
25. Saeed, Y.; Singh, N.; Schwingenschlögl, U. Thickness and strain effects on the thermoelectric transport in nanostructured Bi_2Se_3. *Appl. Phys. Lett.* **2014**, *104*, 2–7. [CrossRef]
26. Wang, F.; Wang, X. Mechanisms in the solution growth of free-standing two-dimensional inorganic nanomaterials. *Nanoscale* **2014**, *6*, 6398–6414. [CrossRef] [PubMed]
27. He, W.; Zhang, G.; Zhang, X.; Ji, J.; Li, G.; Zhao, X. Recent development and application of thermoelectric generator and cooler. *Appl. Energy* **2015**, *143*, 1–25. [CrossRef]
28. Hong, M.; Chen, Z.G.; Yang, L.; Han, G.; Zou, J. Enhanced Thermoelectric Performance of Ultrathin Bi_2Se_3 Nanosheets through Thickness Control. *Adv. Electron. Mater.* **2015**, *1*, 1–9. [CrossRef]
29. Gayner, C.; Amouyal, Y. Energy Filtering of Charge Carriers: Current Trends, Challenges, and Prospects for Thermoelectric Materials. *Adv. Funct. Mater.* **2020**, *30*, 1901789. [CrossRef]
30. Green, A.J.; Dey, S.; An, Y.Q.; O'Brien, B.; O'Mullane, S.; Thiel, B.; Diebold, A.C. Surface oxidation of the topological insulator Bi_2Se_3. *J. Vac. Sci. Technol. A Vacuum Surfaces Films* **2016**, *34*, 061403. [CrossRef]
31. Das, L.; Guleria, A.; Adhikari, S. Aqueous phase one-pot green synthesis of SnSe nanosheets in a protein matrix: Negligible cytotoxicity and room temperature emission in the visible region. *RSC Adv.* **2015**, *5*, 61390–61397. [CrossRef]
32. Shen, J.; Chen, Z.; Lin, S.; Zheng, L.; Li, W.; Pei, Y. Single Parabolic Band Behavior of Thermoelectric P-Type $CuGaTe_2$. *J. Mater. Chem. C* **2015**, *4*, 209–214. [CrossRef]
33. Luo, Z.Z.; Cai, S.; Hao, S.; Bailey, T.P.; Hu, X.; Hanus, R.; Ma, R.; Tan, G.; Chica, D.G.; Snyder, G.J.; et al. Ultralow Thermal Conductivity and High-Temperature Thermoelectric Performance in n-Type $K_{2.5}Bi_{8.5}Se_{14}$. *Chem. Mater.* **2019**, *31*, 5943–5952. [CrossRef]
34. Samanta, M.; Pal, K.; Pal, P.; Waghmare, U.V.; Biswas, K. Localized Vibrations of Bi Bilayer Leading to Ultralow Lattice Thermal Conductivity and High Thermoelectric Performance in Weak Topological Insulator n-Type BiSe. *J. Am. Chem. Soc.* **2018**, *140*, 5866–5872. [CrossRef]
35. Jia, F.; Liu, Y.Y.; Zhang, Y.F.; Shu, X.; Chen, L.; Wu, L.M. Bi_8Se_7: Delocalized Interlayer π-Bond Interactions Enhancing Carrier Mobility and Thermoelectric Performance near Room Temperature. *J. Am. Chem. Soc.* **2020**, *142*, 12536–12543. [CrossRef] [PubMed]
36. Zong, P.A.; Zhang, P.; Yin, S.; Huang, Y.; Wang, Y.; Wan, C. Fabrication and Characterization of a Hybrid Bi_2Se_3/Organic Superlattice for Thermoelectric Energy Conversion. *Adv. Electron. Mater.* **2019**, *5*, 1–8. [CrossRef]
37. Dun, C.; Hewitt, C.A.; Huang, H.; Xu, J.; Zhou, C.; Huang, W.; Cui, Y.; Zhou, W.; Jiang, Q.; Carroll, D.L. Flexible n-type thermoelectric films based on Cu-doped Bi_2Se_3 nanoplate and Polyvinylidene Fluoride composite with decoupled Seebeck coefficient and electrical conductivity. *Nano Energy* **2015**, *18*, 306–314. [CrossRef]